Molecular Imaging by Optically Detected Electron Spin Resonance of Nitrogen-Vacancies in Nanodiamonds

Alex Hegyi* and Eli Yablonovitch

Department of Electrical Engineering and Computer Sciences, University of California, Berkeley, California 94720, United States

Ⓢ *Supporting Information*

ABSTRACT: We propose a novel biomedical imaging technique, called nanodiamond imaging, that noninvasively records the three-dimensional distribution of biologically tagged nanodiamonds in vivo. Our technique performs optically detected electron spin resonance of nitrogen-vacancy centers in nanodiamonds, a nontoxic nanomaterial that is easily biologically functionalized. We demonstrate the feasibility of the technique by imaging multiple nanodiamond targets within pieces of chicken breast; it is the first demonstration of imaging within scattering tissue by optically detected magnetic resonance. We achieve a sensitivity equivalent to 740 pg of nanodiamond in 100 s of measurement time and a spatial resolution of 800 μm over a 1 cm^2 field of view, and we show how the technique has the potential to yield images with combined high sensitivity (~100 fg nanodiamond) AND high spatial resolution (~100 μm) over organism-scale fields of view, features which are mutually exclusive in existing imaging modalities except at the shallowest imaging depths.

KEYWORDS: *Medical imaging, nitrogen-vacancy center, fluorescent nanodiamond, optically detected magnetic resonance, tomography*
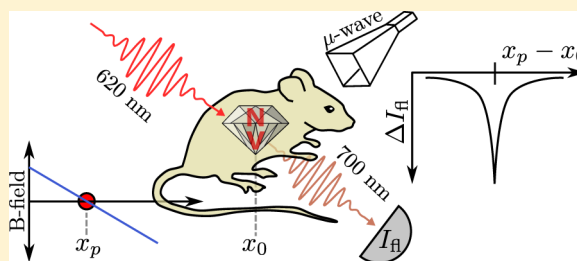
Molecular imaging refers to a class of noninvasive biomedical imaging techniques with the sensitivity and specificity to image biochemical variations in vivo.[1] Molecular imaging modalities typically rely on the use of a contrast agent that highlights a particular biochemical variation and is sensitively detected by an imaging system. We propose a novel molecular imaging approach, called nanodiamond imaging, that uses nanodiamonds containing nitrogen-vacancy (NV) color centers[2−4] as a contrast agent. Nanodiamonds can be tagged with biologically active molecules so they bind to specific receptors;[5−8] their distribution can then be quantified in vivo via optically detected magnetic resonance of the NVs. In effect, our imaging approach can be thought of as optically-detected functional-electron-spin-resonance-imaging, OD-*f*-ESRI. By combining optical detection with magnetic resonance, nanodiamond imaging has the potential to achieve a combination of high sensitivity and high spatial resolution over organism-scale fields of view, features which are mutually exclusive in existing biomedical imaging modalities except at the shallowest imaging depths. It is absent of the complications of ionizing radiation, and the cost should be similar to all-optical imaging. Because nanodiamond imaging is limited by the depth of optical penetration into tissue[9] to depths of a few centimeters, nanodiamond imaging should open up new avenues of investigation for applications where high depth penetration is not required, such as in small-animal imaging,[10,11] tumor margin imaging,[12] sentinel lymph node mapping,[8,13] and perhaps mammography.

Nanodiamond imaging exploits a serendipitous combination of many physical properties of its NV-nanodiamond imaging agent. The first set of useful physical properties come from the nanodiamond host. Nanodiamonds are an ideal nanoparticle for imaging because of their low cost, scalable fabrication methods, nontoxicity, and the facility with which their surfaces can be modified to attach to various biomolecules,[5−8,14] providing a robust method of generating biological specificity. The inclusion of NVs, which are a type of point defect, in the nanodiamonds transforms them into sensitive optical and magnetic probes.

By themselves, the optical properties of the NV are amenable to biological imaging. The fluorescence spectrum of the NV extends from ~630 nm to ~800 nm, peaking around 700 nm, and roughly matching the near-infrared window in biological tissue.[9] The fluorescence has a high quantum yield, is stable (i.e., does not bleach or blink), and occurs at a time scale ($\tau \approx$ 17 ns, in nanodiamond[15]) significantly longer than biological autofluorescence lifetimes such that time-gating enhances the signal-to-noise ratio.[16] These characteristics have created interest in using NV-containing nanodiamonds as fluorescent probes for biology,[15,17] as a replacement for toxic quantum dots and bleachable organic dyes.

The high magnetic sensitivity of the NV also comes from the diamond host. The NV's energy levels exist in the diamond bandgap, so the NV acts like an isolated atom. Its unpaired electrons give rise to a triplet ground state, and because this state is weakly coupled to the diamond lattice, it has long spin

relaxation (T_1) and spin coherence (T_2) lifetimes, or narrow electron spin resonance (ESR) linewidths, even at room temperature (typical values for NV in nanodiamond might be $T_1 \approx 0.1{-}1$ ms and $T_2 \approx 1$ μs[18]). However, the significance of the NV is due to the interaction of its optical and magnetic properties: the spin state can be polarized and detected optically, even for a single NV at room temperature (notably, these features make the NV a prime qubit candidate for quantum computation[19,20]).

The narrow ESR linewidths provide high spatial resolution in a magnetic gradient, while the optical detection provides high measurement sensitivity; many have recognized the significance of this combination for biological applications. NV-based optically detected ESR has a high enough spatial resolution and sensitivity that nanodiamond magnetometers[21,22] based on this principle have been proposed as detectors to perform nanoscale magnetic resonance imaging of biological molecules or probing of biologically relevant spins; recently, imaging the nanoscale magnetic field of a single electronic spin was demonstrated using an NV-based probe in ambient conditions.[23] In combination with the stable fluorescence, the spin properties of the NV allow high resolution localization and tracking of NV-nanodiamonds in live cells.[24,25] Nanodiamond position can also be controlled with nanometer precision in an aqueous environment using optical tweezers while ESR experiments are performed.[26] NVs show promise as monitors of real-time ion channel activity with millisecond time resolution by observing the NV decoherence,[27] as well as sensitive, high spatial resolution wide-field imagers of both magnetic spin labels[28] and of high-speed neural function.[29,30] When NV-nanodiamonds are used as fluorescent markers for microscopy, their fluorescence signal can be modulated via ESR for isolation from background autofluorescence.[31]

However, what we propose, imaging the nanodiamond concentration within the scattering tissue of macroscopic organisms, differs significantly from the existing work. To our knowledge, this is the first report of combining optical detection with magnetic resonance for high-resolution imaging within scattering tissue, though a similar technique utilizing a nonresonant magnetic field effect, magnetofluorescence imaging,[32] has been proposed. Because we aim to illuminate a large fraction of an organism, we are constrained to using a relatively low optical intensity; much of the existing work took advantage of microscopic fields of view and clear optical access to the NVs to get high optical intensity in a focused laser spot.

As an overview of our particular version of optically detected ESR, we make use of a magnetic field-free point, where only those NVs near the field-free point are resonant with a microwave field at 2.869 GHz. Optical excitation polarizes the NV spins into a highly fluorescent state, and the microwaves mix only those spins near the field-free point into a less fluorescent state. Thus, the microwaves decrease the fluorescence by an amount proportional to the nanodiamond concentration at the field-free point. By sweeping the field-free point across an organism and tracking the changes in fluorescence, a quantitative map of the nanodiamond concentration as a function of position can be obtained.

Critical to the functioning of nanodiamond imaging are the NV's properties of optically induced spin polarization and optical spin detection. As shown in Figure 1a and b, the electronic ground state of the NV is a spin triplet, with a zero-magnetic-field splitting of 2.869 GHz between the $m_s = 0$ and the $m_s = \pm 1$ sublevels. The NV spin is pumped into the $m_s = 0$
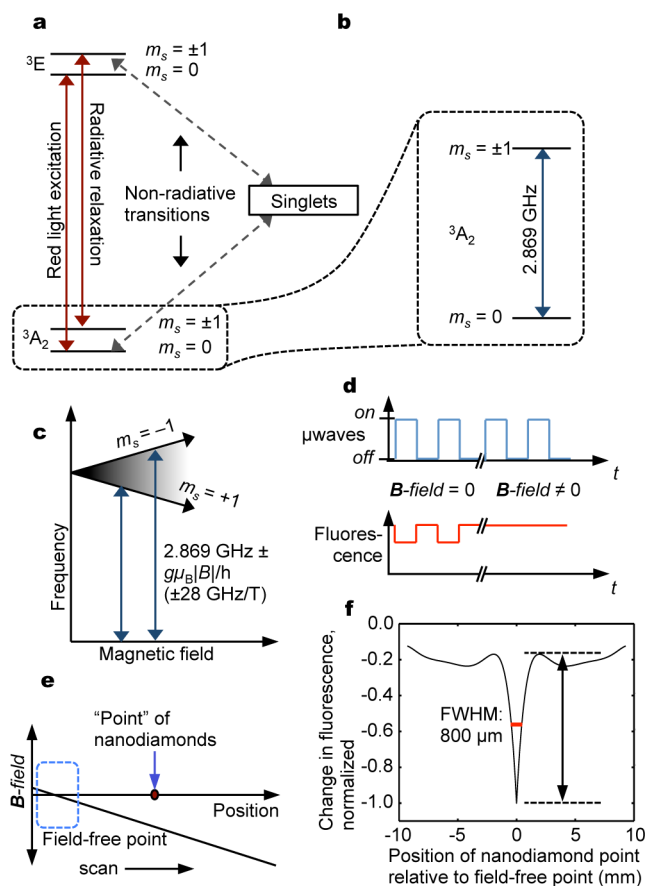
Figure 1. NV optical transitions lead to optically induced spin pumping and optically detectable spin state. (a) Electronic level structure of the NV, depicting spin-conserving radiative transitions as well as nonradiative transitions, through singlet states, from $m_s = \pm 1$ to $m_s = 0$. Upon optical cycling the spin ends up in the $m_s = 0$ state, which fluoresces brighter than the $m_s = \pm 1$ states. (b) The 2.869 GHz transition between $m_s = 0$ and $m_s = \pm 1$, in the absence of magnetic field (or strain). (c) A magnetic field along the NV spin axis splits the spin transitions; in nanodiamond powder, transitions occur at all frequencies (indicated by the grayscale) in between the two extreme frequencies, because of the random orientations of the nanodiamonds relative to the field. (d) Under optical excitation, chopping 2.869 GHz microwaves produces a synchronous modulation in fluorescence at the chopping frequency, but only in the absence of a magnetic field. (e, f) Scanning a field-free point across a point of nanodiamonds (e) with microwaves on and tracking the fluorescence yields the imaging point-spread function (f). The height of the central peak, indicated by the two dashed lines with a fwhm of 800 μm, is 87% of the full height.

sublevel upon optical excitation, because the intermediate singlet states decay preferentially to the $m_s = 0$ sublevel. Furthermore, because the $m_s = \pm 1$ can decay nonradiatively while the $m_s = 0$ decays only radiatively, $m_s = \pm 1$ fluoresces more dimly than $m_s = 0$. Microwaves resonant with the spin transitions mix the spin sublevels, and by placing a magnetic field along the NV axis (Figure 1c), the ± 1 spin sublevels split relative to each other at a rate of 56 GHz T^{-1} (approximately equivalent to the Zeeman splitting of a free electron). In nanodiamond powder, transitions at all frequencies between the two extreme frequencies occur because of the random orientation of individual nanodiamonds with respect to the magnetic field.

After optical pumping of the NV spins into the bright $m_s = 0$ sublevel, microwaves at 2.869 GHz mix the spin sublevels,

leading to an observable decrease in fluorescence, but only in the *absence* of a magnetic field (Figure 1d), that is, at the field-free point. Thus, the concentration of nanodiamonds at the field-free point can be inferred by the decrease in intensity of the NV fluorescence. As the field-free point is scanned in one dimension across a point of nanodiamonds (Figure 1e), we obtain the point-spread function (PSF) for our imaging system (Figure 1f); Supporting Information 3 describes in detail how we obtained this.

To image a 2D slice or a 3D volume of the nanodiamond concentration within an organism, we can scan the field-free point across it in two or three dimensions. Two-dimensional projections of the nanodiamond concentration can be obtained with a field-free line; projections from different angles can be combined into a 3D image using a standard reconstruction algorithm, as in computed tomography. Forming a 3D image in this way will generally lead to higher SNR in the same measurement time than 3D scanning of a field-free point, because the measurement is multiplexed (i.e., information pertinent to many voxels is sampled at once).

The use of a field-free point or line, as inspired by *x*-space magnetic particle imaging,[33] distinguishes this kind of spin resonance imaging from traditional MRI. MRI relies on the coherent precession of spins, within a magnetic gradient, across the sample volume. In nanodiamond imaging, the 2.869 GHz zero-field splitting of the triplet levels acts as an effective magnetic field directed along the diamond's [111] crystalline axis, yet the orientation of this effective magnetic field relative to any applied gradient is arbitrary, and it creates an uncertainty in the precession frequency of the various NV spins. However, the advantage of working at the field-free point is the resonance frequency only depends on the crystal field, which is independent of the nanodiamond orientation. The gradient that surrounds the field-free point smears out the resonance, but that is acceptable because it does so predictably.

A detailed description of the imaging system (Figure 2) can be found in Supporting Information 1. Briefly, a red LED attached to a current source provides stable optical excitation at 610−630 nm and generates ~1 W cm^{-2} of red light at the sample (the NV optical transition saturates around 10^6 W cm^{-2}[15]). Fluorescence is detected by a single photodiode; note that positional information about the nanodiamonds is completely encoded into the fluorescence intensity and not spatially resolved at the detector, although using a multielement detector may provide additional information for image reconstruction. Four permanent magnets in a cylindrical quadrupolar arrangement create a field-free line at the center of a 1 T m^{-1} gradient, for 2D projection imaging along the *z*-axis. The line can be shifted relative to the sample via a dipolar arrangement of electromagnets in the *x*- and *y*-axes to form images with a 1 cm^2 field of view. The microwaves are modulated at 379 Hz, and the corresponding change in fluorescence is synchronously detected. The change in signal from turning the microwaves on and off is on the order of 0.1%.

Many images of nanodiamond phantoms inside 1 cm × 1 cm × 2 cm pieces of chicken breast, which may be a good surrogate for human breast tissue due to its similar optical properties,[34] were taken to demonstrate the imaging technique. All phantoms were made out of double-sticky tape covered with a ~4 μg mm^{-2} areal density of nanodiamonds, as discussed in Supporting Information 2. Shown in Figure 3 are photographs of the phantoms (a), a diagram and photograph of the chicken breast during the experiment (b), the raw images and
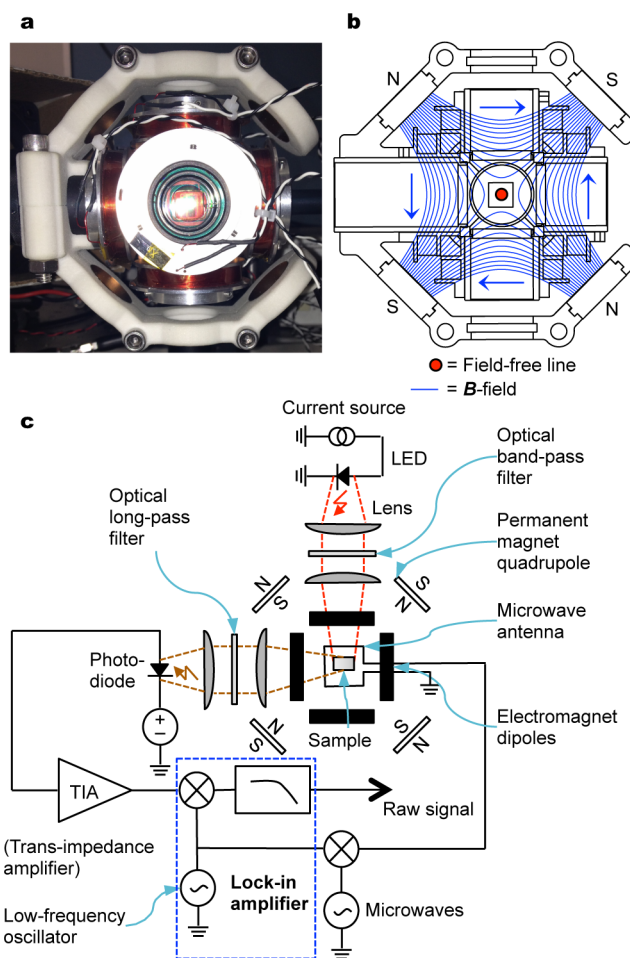
Figure 2. Nanodiamond imaging apparatus. (a) Photo of the apparatus. Permanent magnets are held by the white arms; electromagnet coils (copper wire) are visible as well. (b) Cross-section of the imaging apparatus showing orientation of permanent magnets. The square in the middle is the 1 cm × 1 cm field of view. (c) A schematic of the imaging system.

deconvolved images of the phantom outside of chicken breast obtained from the imaging system (c), raw and deconvolved images of the phantom under 5 mm of chicken (d; also the situation depicted in b), and for the "L" phantom under 12 mm of chicken (e). Note no change in resolving power with depth, as expected. Also, once inside the chicken breast, a human observer can no longer see the phantoms, so there is some rotation of the phantom relative to the images of the phantoms outside of the chicken. The PSF in Figure 3f is obtained from revolving the PSF in Figure 1f. In Figure 3g, we show a line scan through the raw and deconvolved images of the "A" as indicated in Figure 3c and compare it to a line scan through a model of our phantom (representing a ground truth image) and through a simulated raw image of the phantom model. An advantage of our imaging technique is its transparency: the raw image data reveals the basic structure of the nanodiamond distribution, and tomography or inversion of an imaging system model (in this case, represented by deconvolution) is not required to present the data in a visually useful form. However, deconvolution by the PSF produces an image that is essentially a maximum likelihood estimate of the nanodiamond distribution within the sample.
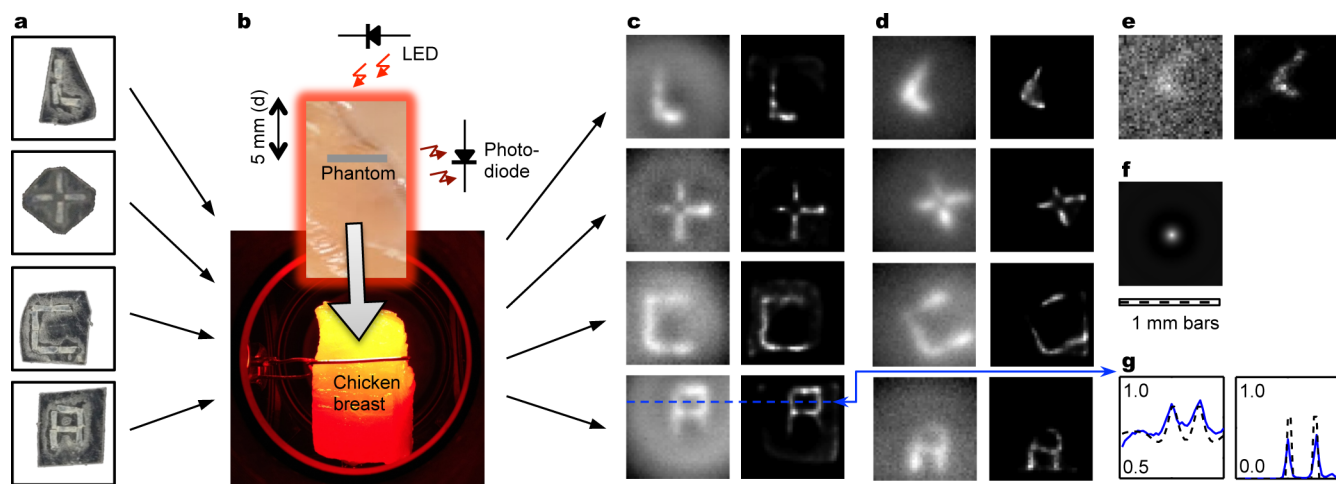
Figure 3. A summary of the data. (a) Nanodiamond phantoms made of double-sticky tape and nanodiamonds, shown at the same scale as the rest of the images. (b) The gray stripe on the piece of chicken breast represents the edge of the phantom, which is placed inside the chicken breast, 5 mm back from the front surface, facing the LED. Fluorescence is collected off to the side. Also shown is the actual piece of chicken breast illuminated by the LED. (c) The phantoms imaged outside of chicken breast, both before (left) and after (right) deconvolution by the point-spread function. (d) Same as c but under 5 mm chicken breast. (e) Image of the "L" phantom under 12 mm chicken breast, before and after deconvolution. (f) Point-spread function. All images are shown with a linear grayscale lookup table that spans the full range of the data in each image. (g) Line scan through the raw image (left) and the deconvolved image (right) of the "A" phantom (solid blue lines); the dashed black line (left) represents the simulated raw image of the phantom, and it was generated by convolving a model of the phantom (dashed black line, right) with the PSF.

The resolution of this particular imaging system depends on the width of the PSF, which varies inversely with the strength of the magnetic field gradient. With a 1 T m^{-1} gradient, the central peak of the PSF (indicated on Figure 1f) has a fwhm of roughly 800 μm. As calculated in Supporting Information 6, the amplitude of the PSF scales roughly as r^{-1}, where r is the distance from the field-free point to a test point of nanodiamonds, because the fraction of nanodiamonds still resonant with the microwaves also scales as this factor (gradient in Figure 1c). Deviations from this scaling primarily come from strain in the nanodiamonds causing inhomogeneous broadening of the zero-field transition (reducing the maximum modulation of the fluorescence achievable with a single microwave frequency and increasing the width of the PSF), the development of an anticrossing between the $m_s = 1$ and $m_s = -1$ states with applied magnetic field (causing a pronounced first dip) and a lowering in energy of the $m_s = 0$ state at higher magnetic fields (blue-shifting the anticrossing above the microwave frequency and increasing the proportion of NV transitions resonant with the microwaves).

The sensitivity to detect the presence of nanodiamonds at the surface of a tissue sample, measured by introducing a known quantity of nanodiamond into the imaging system and scaling the quantity to a signal-to-noise ratio (SNR) of unity, is 2.2 mM mm^3 Hz$^{-1/2}$. (That is, a 2.2 mM concentration of carbon atoms in a mm^3 voxel can be detected with a SNR of unity in one Hz of measurement bandwidth. This corresponds to a sensitivity of 24 pM mm^3 Hz$^{-1/2}$ in terms of the 100 nm nanodiamonds used in the experiment, or 740 pg of nanodiamond in 100 s of measurement time.) There are many performance enhancements we can expect which would drive sensitivity much higher, more than 7 orders of magnitude in combination, discussed in detail in Supporting Information 4. Most notably, different NV-nanodiamond synthesis techniques may increase the ratio of NVs to carbon atoms: sintering of detonation nanodiamond may increase this ratio to 1%[18], whereas the nanodiamonds used in the current experiment contain 6 ppm NV, introduced by ion implantation

and annealing. Further sensitivity enhancements are expected from pulsing the optical and/or microwave excitation, enhancing the amount of fluorescence collected, time-gating the fluorescence collection, water-cooling the organism to allow higher optical excitation intensity, and reducing nanodiamond strain (which would also produce higher resolution).

For a reference point, it is helpful to make a comparison to existing imaging techniques. In Figure 4, we attempt to compare nanodiamond imaging (NDI) to several contrast agent-based imaging techniques on the basis of sensitivity (in terms of minimum detectable mass of imaging agent), resolution, and cost. The data for existing techniques were obtained from four references, and details of how the graph was
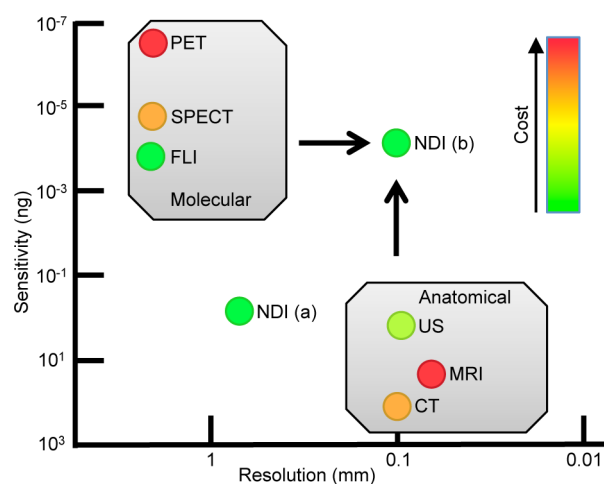
Figure 4. Comparison of nanodiamond imaging to existing techniques. Both the current implementation of nanodiamond imaging (NDI (a)) and future implementation (NDI (b), with 0.03% of potential sensitivity improvements, and reasonable increase in resolution) are compared to popular existing molecular and anatomical imaging techniques, in terms of mass sensitivity, resolution, and cost. FLI: fluorescence imaging; US: ultrasound.

prepared are described in Supporting Information 5. For existing techniques, there is a clear breakdown into two groups: those labeled "Anatomical" for their higher resolution but lower sensitivity (ultrasound (US), magnetic resonance imaging (MRI), and X-ray computed tomography (CT)) and those labeled "Molecular" for their higher sensitivity but lower resolution (positron emission tomography (PET), single photon emission computed tomography (SPECT), and fluorescence-based molecular imaging (FLI)).

The current implementation of NDI (a) has higher mass sensitivity than existing anatomical techniques and higher resolution than the molecular techniques. With 4 orders of magnitude sensitivity improvement (around 0.03% of the identified avenues for improvement), and less than 1 order of magnitude improvement in resolution—possible by increasing the magnetic field gradient or reducing nanodiamond strain— nanodiamond imaging would rival both molecular imaging in terms of sensitivity and anatomical imaging in terms of resolution. The main drawback is the limited depth penetration: the signal attenuates with depth at a rate three times faster than the effective optical attenuation, because the optical excitation must pass through tissue to excite the NVs and generate fluorescence; furthermore, the NV spin polarization, and hence the modulation of the fluorescence achievable with the microwaves, is proportional to the optical excitation; finally, the fluorescence also has to escape from the tissue.

Note a potential simplification of the technique would be to do away with microwaves and perform all-optical imaging by relying on the spin-mixing between the brighter and darker states that occurs at high magnetic fields,[35] such that those NVs within the field-free point fluoresce brightest. However, this approach would significantly degrade the spatial resolution, and it is not easily amenable to modulation schemes. Also, the use of NV-containing nanodiamonds for nanodiamond imaging is incidental; it may turn out that a better material system is identified in the future for performing OD-*f*-ESRI.

ASSOCIATED CONTENT

Ⓢ Supporting Information
Details of apparatus; sample preparation and imaging; processing of raw data: microwave feed-through subtraction, derivation of point-spread function, and subsequent deconvolution; measurement and calculation of sensitivity; creation of Figure 4; understanding the point-spread function. This material is available free of charge via the Internet at http://pubs.acs.org.

AUTHOR INFORMATION

Corresponding Author
*Mailing address: 205 Cory Hall, Berkeley, CA 94720. Telephone: +1-510-643-5801. E-mail: hegyi@eecs.berkeley.edu.

Notes
The authors declare the following competing financial interest(s): Alex Hegyi is an inventor on a provisional patent related to this work.

ACKNOWLEDGMENTS

REFERENCES

(1) James, M. L.; Gambhir, S. S. A Molecular Imaging Primer: Modalities, Imaging Agents, and Applications. *Physiol. Rev.* **2012**, *92*, 897−965.

(2) Budker, D. Diamond Nanosensors: The Sense of Colour Centres. *Nat. Phys.* **2011**, *7*, 453−454.

(3) Awschalom, D. D.; Epstein, R.; Hanson, R. The Diamond Age of Spintronics. *Sci. Am.* **2007**, *297*, 84−91.

(4) Aharonovich, I.; Greentree, A. D.; Prawer, S. Diamond Photonics. *Nat. Photonics* **2011**, *5*, 397−405.

(5) Zhang, X.-Q.; Lam, R.; Xu, X.; Chow, E. K.; Kim, H.-J.; Ho, D. Multimodal Nanodiamond Drug Delivery Carriers for Selective Targeting, Imaging, and Enhanced Chemotherapeutic Efficacy. *Adv. Mater.* **2011**, *23*, 4770−5.

(6) Schrand, A.; Hens, S. A. C.; Shenderova, O. Nanodiamond Particles: Properties and Perspectives for Bioapplications. *Crit. Rev. Solid State Mater. Sci.* **2009**, *34*, 18−74.

(7) Chao, J.-I.; Perevedentseva, E.; Chung, P.-H.; Liu, K.-K.; Cheng, C.-Y.; Chang, C.-C.; Cheng, C.-L. Nanometer-sized Diamond Particle as a Probe for Biolabeling. *Biophys. J.* **2007**, *93*, 2199−208.

(8) Vaijayanthimala, V.; Cheng, P.-Y.; Yeh, S.-H.; Liu, K.-K.; Hsiao, C.-H.; Chao, J.-I.; Chang, H.-C. The Long-term Stability and Biocompatibility of Fluorescent Nanodiamond as an in Vivo Contrast Agent. *Biomaterials* **2012**, *33*, 7802−7794.

(9) Tuchin, V. *Tissue Optics: Light Scattering Methods and Instruments for Medical Diagnosis*, 1st ed.; SPIE Publications: Bellingham, WA, 2000; p 9.

(10) Kemp, R. A. de; Epstein, F. H.; Catana, C.; Tsui, B. M. W.; Ritman, E. L. Small-animal Molecular Imaging Methods. *J. Nucl. Med.* **2010**, *51* (Suppl 1), 18S−32S.

(11) Meikle, S. R.; Kench, P.; Kassiou, M.; Banati, R. B. Small Animal SPECT and Its Place in the Matrix of Molecular Imaging Technologies. *Phys. Med. Biol.* **2005**, *50*, R45−61.

(12) Patlak, M. Nanoimaging Devices Illuminate Tumor Margins During Surgery. *J. Natl. Cancer Inst.* **2011**, *103*, 173−4.

(13) Bonnema, J.; Velde, C. J.; van de Sentinel, H. Lymph Node Biopsy in Breast Cancer. *Ann. Oncol.* **2002**, *13*, 1531−1537.

(14) Chow, E. K.; Zhang, X.-Q.; Chen, M.; Lam, R.; Robinson, E.; Huang, H.; Schaffer, D.; Osawa, E.; Goga, A.; Ho, D. Nanodiamond Therapeutic Delivery Agents Mediate Enhanced Chemoresistant Tumor Treatment. *Sci. Transl. Med.* **2011**, *3*, 73ra21.

(15) Fu, C.-C.; Lee, H.-Y.; Chen, K.; Lim, T.-S.; Wu, H.-Y.; Lin, P.-K.; Wei, P.-K.; Tsao, P.-H.; Chang, H.-C.; Fann, W. Characterization and Application of Single Fluorescent Nanodiamonds as Cellular Biomarkers. *Proc. Natl. Acad. Sci. U.S.A.* **2007**, *104*, 727−32.

(16) Faklaris, O.; Garrot, D.; Joshi, V.; Druon, F.; Boudou, J.-P.; Sauvage, T.; Georges, P.; Curmi, P. A.; Treussart, F. Detection of Single Photoluminescent Diamond Nanoparticles in Cells and Study of the Internalization Pathway. *Small* **2008**, *4*, 2236−9.

(17) Chang, Y.-R.; Lee, H.-Y.; Chen, K.; Chang, C.-C.; Tsai, D.-S.; Fu, C.-C.; Lim, T.-S.; Tzeng, Y.-K.; Fang, C.-Y.; Han, C.-C.; et al. Mass Production and Dynamic Imaging of Fluorescent Nanodiamonds. *Nat. Nanotechnol.* **2008**, *3*, 284−8.

(18) Baranov, P. G.; Soltamova, A. A.; Tolmachev, D. O.; Romanov, N. G.; Babunts, R. A.; Shakhov, F. M.; Kidalov, S. V; Vul', A. Y.; Mamin, G. V; Orlinskii, S. B.; et al. Enormously High Concentrations of Fluorescent Nitrogen-vacancy Centers Fabricated by Sintering of Detonation Nanodiamonds. *Small* **2011**, *7*, 1533−7.

(19) Kok, P.; Lovett, B. W. Materials Science: Qubits in the Pink. *Nature* **2006**, *444*, 49.

(20) Ladd, T. D.; Jelezko, F.; Laflamme, R.; Nakamura, Y.; Monroe, C.; O'Brien, J. L. Quantum Computers. *Nature* **2010**, *464*, 45−53.

(21) Maze, J. R.; Stanwix, P. L.; Hodges, J. S.; Hong, S.; Taylor, J. M.; Cappellaro, P.; Jiang, L.; Dutt, M. V. G.; Togan, E.; Zibrov, A. S.; et al. Nanoscale Magnetic Sensing with an Individual Electronic Spin in Diamond. *Nature* **2008**, *455*, 644−7.

(22) Balasubramanian, G.; Chan, I. Y.; Kolesov, R.; Al-Hmoud, M.; Tisler, J.; Shin, C.; Kim, C.; Wojcik, A.; Hemmer, P. R.; Krueger, A.; et al. Nanoscale Imaging Magnetometry with Diamond Spins Under Ambient Conditions. *Nature* **2008**, *455*, 648−51.

(23) Grinolds, M. S.; Hong, S.; Maletinsky, P.; Luan, L.; Lukin, M. D.; Walsworth, R. L.; Yacoby, A. Nanoscale Magnetic Imaging of a Single Electron Spin Under Ambient Conditions. *arXiv:1209.0203*, **2012**.

(24) Shin, C.; Kim, C.; Kolesov, R.; Balasubramanian, G.; Jelezko, F.; Wrachtrup, J.; Hemmer, P. R. Sub-optical Resolution of Single Spins Using Magnetic Resonance Imaging at Room Temperature in Diamond. *J. Lumin.* **2010**, *130*, 1635−1645.

(25) McGuinness, L. P.; Yan, Y.; Stacey, A.; Simpson, D. A.; Hall, L. T.; Maclaurin, D.; Prawer, S.; Mulvaney, P.; Wrachtrup, J.; Caruso, F.; et al. Quantum Measurement and Orientation Tracking of Fluorescent Nanodiamonds Inside Living Cells. *Nat. Nanotechnol.* **2011**, *6*, 358−63.

(26) Horowitz, V. R.; Alemán, B. J.; Christle, D. J.; Cleland, A. N.; Awschalom, D. D. Electron Spin Resonance of Nitrogen-vacancy Centers in Optically Trapped Nanodiamonds. *Proc. Natl. Acad. Sci. U.S.A.* **2012**, *109*, 13493−7.

(27) Hall, L. T.; Hill, C. D.; Cole, J. H.; Städler, B.; Caruso, F.; Mulvaney, P.; Wrachtrup, J.; Hollenberg, L. C. L. Monitoring Ion-channel Function in Real Time Through Quantum Decoherence. *Proc. Natl. Acad. Sci. U.S.A.* **2010**, *107*, 18777−82.

(28) Steinert, S.; Ziem, F.; Hall, L.; Zappe, A.; Schweikert, M.; Aird, A.; Balasubramanian, G.; Hollenberg, L.; Wrachtrup, J. Magnetic Spin Imaging Under Ambient Conditions with Sub-cellular Resolution. *arXiv:1211.3242*, **2012**.

(29) Pham, L. M.; Sage, D.; Le; Stanwix, P. L.; Yeung, T. K.; Glenn, D.; Trifonov, A.; Cappellaro, P.; Hemmer, P. R.; Lukin, M. D.; Park, H.; et al. Magnetic Field Imaging with Nitrogen-vacancy Ensembles. *New J. Phys.* **2011**, *13*, 045021.

(30) Hall, L. T.; Beart, G. C. G.; Thomas, E. A.; Simpson, D. A.; McGuinness, L. P.; Cole, J. H.; Manton, J. H.; Scholten, R. E.; Jelezko, F.; Wrachtrup, J.; et al. High Spatial and Temporal Resolution Wide-field Imaging of Neuron Activity Using Quantum NV-diamond. *Sci. Rep.* **2012**, *2*, 401.

(31) Igarashi, R.; Yoshinari, Y.; Yokota, H.; Sugi, T.; Sugihara, F.; Ikeda, K.; Sumiya, H.; Tsuji, S.; Mori, I.; Tochio, H.; et al. Real-time Background-free Selective Imaging of Fluorescent Nanodiamonds in Vivo. *Nano Lett.* **2012**, *12*, 5726−32.

(32) Yang, N.; Cohen, A. E. Optical Imaging Through Scattering Media via Magnetically Modulated Fluorescence. *Opt. Express* **2010**, *18*, 25461.

(33) Goodwill, P. W.; Conolly, S. M. The X-space Formulation of the Magnetic Particle Imaging Process: 1-D Signal, Resolution, Bandwidth, SNR, SAR, and Magnetostimulation. *IEEE Trans. Med. Imaging* **2010**, *29*, 1851−9.

(34) Das, B. B.; Liu, F.; Alfano, R. R. Time-resolved Fluorescence and Photon Migration Studies in Biomedical and Model Random Media. *Rep. Prog. Phys.* **1997**, *60*, 227−292.

(35) Tetienne, J.-P.; Rondin, L.; Spinicelli, P.; Chipaux, M.; Debuisschert, T.; Roch, J.-F.; Jacques, V. Magnetic-field-dependent Photodynamics of Single NV Defects in Diamond: Application to Qualitative All-optical Magnetic Imaging. *arXiv:1206.1201*, **2012**.